Electronic descriptors for vacancy formation and hydrogen solution in Be-rich intermetallics

Keisuke Mukai,[1*] Ryuta Kasada,[2] Jae-Hwan Kim,[3] Masaru. Nakamichi[3]

[1] Institute of Advanced Energy, Kyoto University, Gokasho, Uji, Kyoto 611-0011, Japan

[2] Institute for Material Research, Tohoku University, 2-1-1 Katahira, Aoba-ku, Sendai 980-8577, Japan

[3] Fusion Energy Research and Development Directorate, National Institutes for Quantum Science and Technology, 2-166 Obuchi, Omotedate, Rokkasho, Aomori, 039-3212, Japan

*Corresponding author: k-mukai@iae.kyoto-u.ac.jp

Keywords: *Band theory, defects, hydrogen solution, ab-initio calculations, nuclear fusion*

Abstract

The use of an electronic descriptor is a high-throughput approach for predicting the chemical reactivities of various materials that has the potential to significantly facilitate the material design of Be intermetallic neutron multipliers for nuclear fusion applications. However, electronic descriptors for Be intermetallics with the desired properties, including radiation tolerance and reduced hydrogen retention, have been poorly understood. Herein, we perform first-principles calculations on 42 existing binary Be intermetallics to find an effective electronic descriptor. We demonstrate that the occupied Be *p* band center referenced with the Fermi level is a bulk descriptor, correlating with the Be vacancy formation energy; a positive and linear correlation with correlation factor R^2 = 0.85 was observed for $Be_{12}X$ (X: transition metal). The upward shift in energy of the occupied Be *p* states with early or middle transition metals can reduce hydrogen solution energy, which could be attributed to the less filled anti-bonding state of interstitial hydrogen atom. It is confirmed that the bulk descriptor is an experimentally measurable scale, having the strong linearity (R^2 = 0.97) with the calculated; therefore, it can accelerate the material development of beryllium intermetallic neutron multipliers.

1. Introduction

The band theory, based on the model proposed by Hammer and Norkov,[1–3] has enabled the first-principles search for functional materials with desired chemical properties. The *d* band center referenced to the Fermi level, which is defined as a centroid of projected density of state (PDOS) onto metal atoms, is an electronic descriptor that correlates with the catalytic activities of precious metal alloys. While the model and descriptors have been further improved for a better description,[4–6] the *d* band theory is simultaneously utilized to understand experimental results of oxygen evolution reaction, oxygen reducing reaction, and hydrogen evolution reaction for fuel cells and electrolysis of water.[7–10] More recently, the use of electronic descriptors has been expanded to predict the chemical reactivities of metal oxides and sulfides.[11,12] For perovskite oxides, it has been shown that O *p* band center referenced with Fermi level in metal oxide bulk is correlated with oxygen reduction/evolution reaction activity,[13–16] vacancy formation energy,[13,17,18] ion migration barrier,[13] and oxygen storage capacity.[19]

Beryllium is a light metal element ($Z = 4$) that has no *d* band. With various elements, Be forms intermetallics (beryllides) exhibiting metallic character in most cases. Nuclear fusion is a sustainable and low-carbon energy source, in which Li-containing ceramics (tritium breeder) and Be compounds (neutron multiplier) are packed together in solid breeding blanket to breed fuel tritium efficiently and sufficiently.[20,21] Be-rich beryllides have attracted increasing attention as a substitute of pure Be metal because the low chemical reactivity with steam can significantly reduce hydrogen generation by two orders of magnitude in a loss-of-coolant accident.[22],[23] To achieve a fuel self-sufficiency (tritium breeding ratio > 1),[24] a beryllide with a high Be atomic density as

well as minimum radio-activation is desired. Tritium, a radioactive isotope of hydrogen, is produced in the multiplier bulk as a result of transmutations. Another attractive aspect of a beryllide neutron multiplier is its character of low hydrogen isotope retention, including less amount of hydrogen retention, lower activation energy for the desorption, lower temperature for hydrogen release than Be metal.[25–27] These properties are promising because it reduces tritium inventory in a fusion reactor compared with Be metal and makes material handling easier during the decommissioning process. Particularly, hydrogen binding within bulk plays a key role in the release of tritium as the rate limiting diffusion barriers are comparable between Be and $Be_{12}Ti$.[28] Previous computational studies using density functional theory (DFT) calculations[29,30] have reported the lower energetic costs of hydrogen solution in $Be_{12}Ti$ and $Be_{12}V$ bulks, suggesting an easier dissolution of tritium from the crystal bulks. However, it is still unclear why beryllide compounds release hydrogen isotopes so easily and have reduced energy costs for hydrogen solution.

For fusion applications, the binary phase ($Be_{12}Ti$, $Be_{12}V$, and $Be_{13}Zr$)[22],[25–27,29,31,32] and ternary phase beryllides (Be–Ti–V, Be–Ti–Zr, and Be–Ti–V)[33–35] have been fabricated to characterize the swelling, hardness, oxidation tolerance, and embrittlement by neutron irradiation. Additionally, the fundamental properties of $Be_{12}Mo$, $Be_{12}W$, and Be–Fe–Al compounds have been assessed computationally.[36–38] Nevertheless, such developments of beryllides have been limited not only by the toxicity of Be dust in manufacturing process, but also by time-consuming and expensive neutron irradiation tests performed using research reactors. Our previous experiments using soft X-ray emission spectroscopy (SXES) have shown that the valence electron structure of Be *p* states are largely altered in the intermetallic bulks of $Be_{12}Ti$ and $Be_{12}V$, suggesting

a possible change in the bonding nature of Be.[39] The use of a band model may significantly facilitate the design and development of Be intermetallics; however, electronic descriptors related to the required properties have been poorly understood up till date. Herein, PDOS calculations were systematically carried out on 42 existing binary beryllides to find an effective electronic descriptor. Vacancy formation energy of Be atom and hydrogen solution energy were chosen as measures for defect formation and hydrogen retention properties, respectively. The results show that the occupied Be *p* band center is an experimentally measurable electronic descriptor that correlates with both Be vacancy formation energy and hydrogen solution energy for $Be_{12}X$ (X = Ti, V, Cr, Mn, Fe, Co, Nb, Mo, Pd, Ag, Ta, W, Pt, and Au) compounds.

2. Methods

Experimental

The $Be_{13}Zr$ sample was prepared by plasma-sintering method,[32] using Be (Materion Brush, USA, 99.4 wt.%) and Zr (Kojundo Chemical Laboratory 98 wt.%) powders. The powders were mixed at an atomic ratio of 92.9% Be and 7.1% Zr. The mixture of the powders was cold-pressed and then plasma-sintered at 1050 °C for 20 min under 50 MPa. X-ray diffraction (XRD) using Co-*K*α confirmed the formation of a single phase of $Be_{13}Zr$ with the space group of $Fm\bar{3}c$, as shown in Fig. S1 in Supporting Information (SI). The XRD pattern was analyzed using the RIETAN-FP software.[40] Le Bail analysis using the partial structure gave a refined lattice parameter of a = 10.0396(1) Å. The SXES spectrum was obtained by a JXA-8500F field-emission electron probe micro-analyzer (EPMA) by JEOL with an acceleration voltage of 15 kV. A diffraction grating of JS200N was employed where the energy range was 50−210 eV with an energy resolution as good as 0.2 eV.[41] The SXES Be–*K*α spectra from the Be metal, $Be_{12}Ti$,

and $Be_{12}V$ samples were taken from our previous paper.[39]

DFT calculations

DFT calculations were performed using the revised Perdew−Burke−Ernzerhof (RPBE) generalized gradient approximation for the exchange and correlation functional implemented in the Vienna ab initio simulation package (VASP) [42–44]. The used valence electron configuration of Be was $1s^2 2s^2$; namely, both the inner- and outer-shell electrons were involved. In total, electric structures of 42 existing compounds, including $Be_{22}X$ (X = Mo, W, and Re; $Fd\bar{3}m$), $Be_{13}X$ (X = Mg, Ca, Sc, Sr, Y, Zr, and La; $Fm\bar{3}c$) pha), $Be_{12}X$ (X = Ti, V, Cr, Mn, Fe, Co, Nb, Mo, Pd, Ag, Ta, W, Pt, and Au; I_4/mmm), $Be_{17}X_2$ (X = Ti, Zr, and Nb; $R\bar{3}m$), Be_5X (X = Fe, Co, and Pd; $F\bar{4}3m$), Be_5X (X = Sc and Zr; $P6/mmm$), Be_2X (X = V, Cr, Mn, Fe, Mo, and W; $P63/mmc$), Be_2X (X = Ti, Cu, and Nb; $Fd\bar{3}m$), and Be ($P6_3/mmc$), were calculated with a plane-wave cutoff energy of 450 eV. The crystal structure data were taken from the Atom Work database at the National Institute for Materials Science (NIMS).[45] Self-consistency was achieved with a tolerance for a total energy of 10^{-5} eV, and the atomic positions were relaxed until the force was less than 0.02 eV $Å^{-1}$. The cell sizes, number of Be atom sites, and relaxed lattice parameters are listed in Table S1 in SI. The differences between experimental and computational lattice parameters were within 4%. The occupied band center was calculated as the centroid of the filled states, while the whole band center was calculated to be the centroid of DOS in all range of electron energy, including unoccupied states. All the calculated band centers are given with respect to the Fermi energy ε_F. The occupied PDOS of Be below ε_F was convoluted with Gaussian functions with a full width at half-maximum (FWHM) of 1.4 eV. The atomic configurations were depicted by VESTA software.[46]

The formation energy of a Be atomic vacancy at Be*j* site, defined as $E_{V,Bej}$ was obtained using the following equation,

$$E_{V,Bej} = E(Be_{n-1}X_m) + E(Be) - E(Be_nX_m) \quad (1)$$

where E(Be) is the total energy of the perfect Be metal per atom, $E(Be_nX_m)$ is the total energy of the perfect Be_nX_m, and $E(Be_{n-1}X_m)$ is the total energy of $Be_{n-1}X_m$ containing one Be vacancy at Be*j* site, respectively. After calculating the single Be vacancy formation energy for all Be sites, the averaged vacancy formation energy of Be atom, $E_{V,average}$, was obtained by averaging them.

Hydrogen solution energy at interstitial site in $Be_{12}X$ was calculated by using the following equation:

$$E_H = E(Be_nX_mH) - E(Be_nX_m) - 1/2E(H_2) \quad (2)$$

where $E(Be_nX_mH)$ and $E(H_2)$ are the total energies of the system for hydrogen in $Be_{12}X$ and the hydrogen molecule, respectively. The 2×2×1 supercell (52 atoms) was used for $Be_{12}X$; hence n and m were 48 and 4, respectively. One hydrogen atom was placed at the basal tetrahedral site in hexagonal close-packed Be metal,[47] while 3 different interstitial sites for accommodating one interstitial H atom were selected for $Be_{12}X$ bulk (see Section 3.2).

3.1 Vacancy formation in Be intermetallics

The formation of mono-vacancy is a fundamental defect process induced by neutron irradiation and a key indicator of radiation tolerance, while a high Be atomic density is required for achieving efficient neutron multiplification. The vacancy formation of Be atom is the primary focus here because (i) Be is the main constituent element in Be-rich intermetallics, and (ii) Be has a significantly lower vacancy formation energy than an additive element X, as predicted for $Be_{12}X$ (X = Ti, Mo, V, and W).[38]

Fig. 1 shows the Be atomic density plotted with averaged Be vacancy formation energy in Be metal and intermetallics. Although the Be atomic densities decreased by the formation of intermetallic phases, most of the Be intermetallics exhibited higher Be vacancy formation energies than the Be metal, except for $Be_{12}X$ with X being the late transition metals (TMs: X = Co, Pd, Pt, Ag, and Au). Interestingly, Be atomic density was not solely determined by the ratio of Be and X; for example, most of the $Be_{13}X$ compounds had lower Be atomic densities than $Be_{12}X$ despite the higher Be fractions, while the densities of $Be_{22}X$ (X = Mo, W, and Re) were comparable to $Be_{12}X$ with middle 3*d* TMs. Even with the same molar fraction and crystallographic symmetry, these values were greatly altered by the choice of the element X (see $Be_{12}X$ series). Among the $Be_{12}X$ compounds with TMs of group number 5 (i.e., V: $3d^3$, Nb: $4d^3$, and Ta: $5d^3$), the Be atomic density decreased down the group as $Be_{12}V > Be_{12}Nb > Be_{12}Ta$. This is explained by the size of TM's radii, originating from the extended 4*d* and 5*d* states compared with 3*d*. These facts indicate that Be atomic density depends not only on the chemical composition but also on the electronic structure and the packing arrangement of the constituent atoms within the bulk.

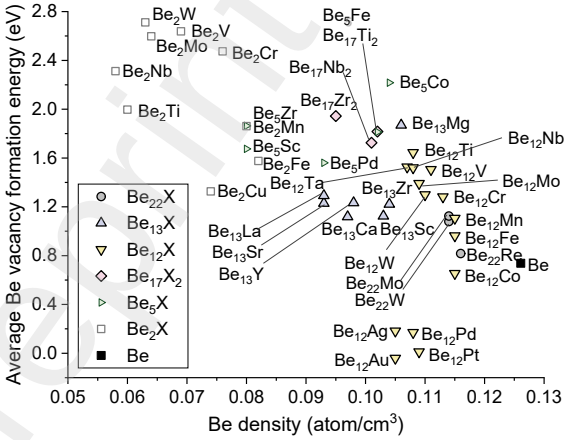

Fig. 1. Plot of Be atomic density with average Be vacancy formation energy of the Be metal and

intermetallic compounds.

The correlation factor (R^2) of each electronic descriptor (occupied and whole band centers) along with the average Be vacancy formation energy in the Be metal and the 42 intermetallic compounds are shown in Fig. 2. The plots are represented in Fig. S2 and S3 in SI, in which a descriptor obtained from PDOS projected onto Be atom at Be*i* site is correlated with the Be vacancy formation energy at the Be site. The strongest correlations were observed in the occupied Be *p* and X *p* band centers, resulting in $R^2 = 0.65$. Overall, the whole band centers had weaker correlations with the Be vacancy formation energy than the occupied. This is contrary to the perovskite system, in which the whole O *p* band center has a slightly better correlation with oxygen vacancy formation energy than the occupied O *p* band center.[15,16] The difference can be understood with the PDOS before and after removing one Be atom from the $Be_{12}Ti$ bulk as illustrated in Fig. S4 in SI. When one Be atom is removed from the bulk and neutral vacancy is formed, electrons are removed from the occupied Be *p* states, mainly from the DOS peak at approximately 2 eV below the Fermi level. Simultaneously, this involves slight changes of X's electronic states because of Be–X bond dissociation. In this process, empty states remain those original electron structure, suggesting that empty states in the Be intermetallics have minor impact on bonding of Be atom, unlike charged oxygen vacancy formation in perovskite involving electron transfer from O to TM (i.e., TM's reduction). Exceptionally, slight change in the unoccupied X *d* states above the Fermi level was observed, which may be the reason why only the whole X *d* band center had a better correlation ($R^2 = 0.24$) than the other whole band centers. Practically, the occupied Be *p* band center is more preferable than the occupied X *d* band center because (1) Be–$K\alpha$ emission appears in a sole energy region (i.e. 100–112 eV) regardless of chemical composition and (2) the

descriptor could be evaluated with a high energy resolution as good as 0.2 eV thanks to the low emission energy.[48] In our previous study, a possible correlation between fully-occupied Be core level (i.e. 1*s* states) and the formation energy of Be mono-vacancy was discussed.[39] The present analysis, however, showed that the centroid of Be core level has a weak correlation with the Be vacancy formation energy (R^2 = 0.34).

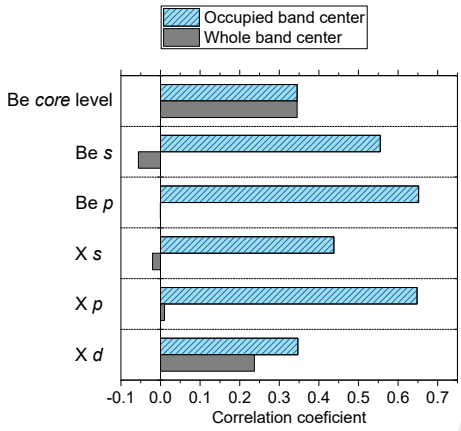

Fig. 2. Correlation coefficient (R^2) between electronic descriptors and Be vacancy formation energy in Be metal and the 42 intermetallic compounds where a negative value represents a negative correlation. The plots of electronic descriptors *vs*. Be vacancy formation energy are represented in Fig. S2 and S3 in Supporting Information (SI).

Fig. 3 shows the valence electron structures of Be, $Be_{12}Ti$, $Be_{12}V$, and $Be_{13}Zr$ bulks. The valence electronic Be *p* states are referenced with the Fermi energy $\varepsilon_{F,DFT}$ in Fig. 3a–d. The occupied Be *p* states of Be metal, $Be_{12}Ti$, $Be_{12}V$, and $Be_{13}Zr$ bulks were convoluted with the Gaussian functions, in which the occupied Be *p* centers were at energy levels of –4.08, –3.32, –3.43, and –3.47 eV, respectively. In Fig. 3e–h, the experimental SXES Be–*K*α spectra were horizontally shifted so that the peak positions were identical to those of the convoluted spectra. The comparison allowed us to determine the experimental energy of Fermi level in the Be–*K*α spectra, $\varepsilon_{F,exp}$. As a result, the

occupied Be *p* band centers referenced $\varepsilon_{F,exp}$ for Be metal, $Be_{12}Ti$, $Be_{12}V$, and $Be_{13}Zr$ samples were evaluated to be –3.92, –3.35, –3.34, and –3.36 eV, respectively. The experimental centroids agreed with those computed within the energy resolution of the SXES (i.e., 0.2 eV). To this end, a strong linear correlation (R^2 = 0.97) between the experimental and computational Be *p* band centers was obtained as shown in Fig. 3i. The energetic upshift in the occupied Be *p* center in the intermetallics is caused by an electronic repopulation driving from the hybridization of the Be *p* states with the partially-occupied *d* states of Ti, V, and Zr as schematically shown in Fig. 3j. A good agreement between the experimental and computational results allows us to employ the occupied Be *p* band center as a sole measure for predicting Be vacancy formation energy. In the following section, we focus on electric descriptors for vacancy formation and hydrogen solution in $Be_{12}X$ because the beryllides have a high Be density, increased vacancy formation energy, and the largest variety of compounds with TMs (i.e., a total of 14 compounds).

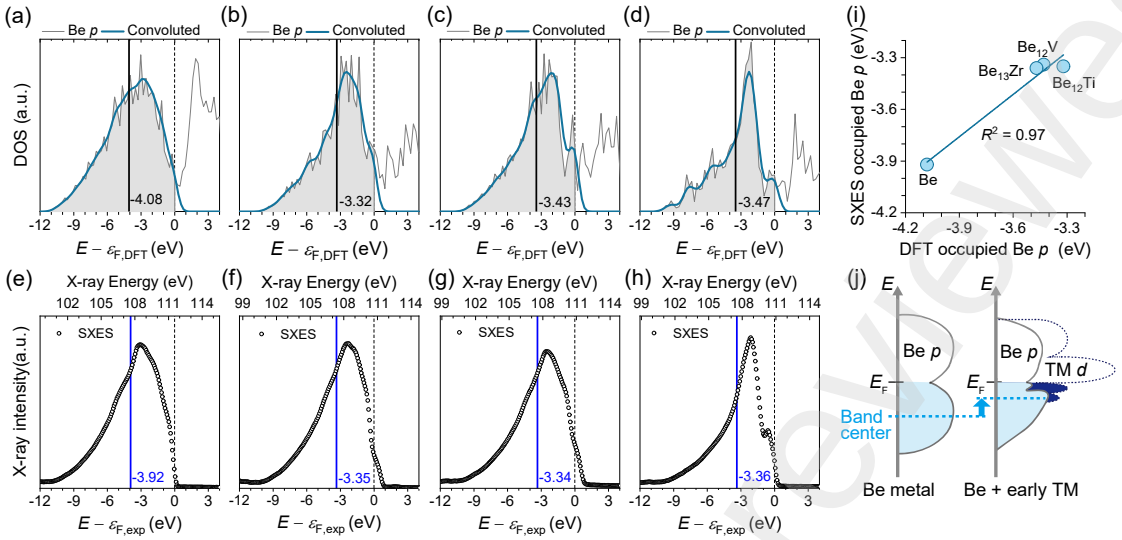

Fig. 3. Computational and experimental Be *p* states by density functional theory (DFT) calculations and soft X-ray emission spectroscopy (SXES). (a–d) Partial density of states (PDOS) of *p* states in Be metal (a), $Be_{12}Ti$ (b), $Be_{12}V$ (c), and $Be_{13}Zr$ bulks (d) with the energy referenced to Fermi energy $\varepsilon_{F,DFT}$, represented with the convoluted spectra of occupied Be *p* states. (e–f) the SXES spectra from the Be metal (e), $Be_{12}Ti$ (f), $Be_{12}V$ (g) and $Be_{13}Zr$ samples (h). (i) Plot of DFT Be *p* band center vs. SXES *p* band center with a linear regression. (j) Schematic PDOS plots of Be metal and intermetallics with an early transition metal (TM) where Be *p* and TM *d* states are drawn with solid and dotted lines. In panel (a–h), dashed and solid lines represent the Fermi energy and the occupied Be *p* band center, respectively.

3. 2 Vacancy formation and hydrogen solution in $Be_{12}X$

Fig. 4 depicts the relationships between the group number of TMs and the Be vacancy formation energy in $Be_{12}X$. Plots of averaged Be vacancy formation energy with occupied Be *p* and whole X *d* band centers are shown in Fig. 5. There are 3 different atomic sites for Be and one for X in $Be_{12}X$ with I_4/mmm space group (Fig. 4a). Atomic coordinates of Be1, Be2, and Be3 sites are (1/4,1/4,1/4), (x,0,0), and (x,1/2,0), respectively, where variations in $E_{V,Bej}$ (j = 1–3) were smaller than 0.15 eV. The calculated Be vacancy formation energies for $Be_{12}Ti$, $Be_{12}V$, $Be_{12}Mo$, and $Be_{12}W$ were confirmed to be in good accordance with the previous computational results.[38] A linear downtrend of Be vacancy formation energy with group number was seen in Fig. 4b.

Similarly, the occupied Be *p* band center exhibited a downtrend with the group number (Fig. 4c), in which group 11 (i.e., Ag and Au) was the outlier from of the line plot. This gradual energetic shift of the occupied *p* states is associated with the increased filling of *d* bands to the right in the TM series and the hybridization between the Be *p* and X *d* states. These trends were observed irrespective of period number of TMs (i.e. 3*d*, 4*d*, or 5*d*) and thus had a strong linear correlation with all of the $Be_{12}X$ compounds (Fig. 5a), which yielded $R^2 = 0.85$. The whole *d* band center of the 3*d* TM locally showed a similar downtrend with the group number, but the plot did not show an overall linear trend. The whole X *d* band center exhibited a weak correlation with Be vacancy formation energy, despite of its very strong linear correlation locally for the 3*d* TM intermetallics ($R^2 = 0.98$) as shown in Fig. 5b. This result suggests an indirect influence of extension of *d* states (i.e., the size of coupling matrix element) on the occupied Be *p* states and consequently indicates that the whole *d* band center is not a suitable scale for predicting the Be vacancy formation energy. The calculated values of $E_{V,average}$ of the $Be_{12}X$ intermetallics with early TMs (X = Ti, V, Nb, and Ta) were 1.51–1.65 eV, which were significantly higher than that of Be metal (0.74 eV). This indicates that higher energy cost is needed to form Be vacancy in the intermetallics with early TMs, as Be atom is strongly bounded with neighbor atoms. Interestingly, it is found that the positive dependency of Be vacancy formation energy with occupied Be *p* band center (Fig. 5a) is inverse to that of oxygen vacancy formation energy with the O *p* band center for perovskite oxides.[13,17]

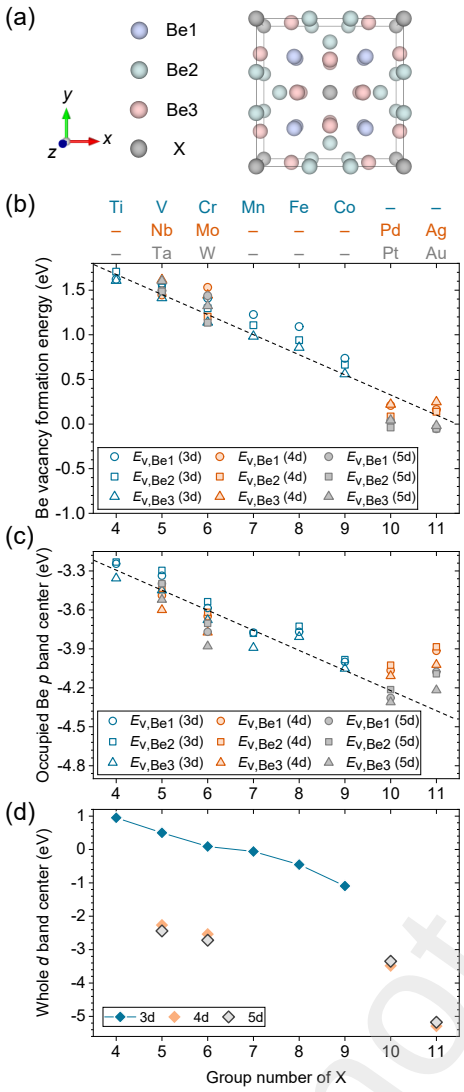

Fig. 4. (a) Unit cell of $Be_{12}X$ (space group: I_4/mmm) including three distinct sites of Be and one site of guest element X. (b–d) Variations of Be vacancy formation energy (b), occupied Be *p* band center (c), and whole X *d* band center (d) in $Be_{12}X$ (X = Ti, V, Cr, Mn, Fe, Co, Nb, Mo, Pd, Ag, Ta, W, Pt and Au) bulk as a function of the group number of transition metals.

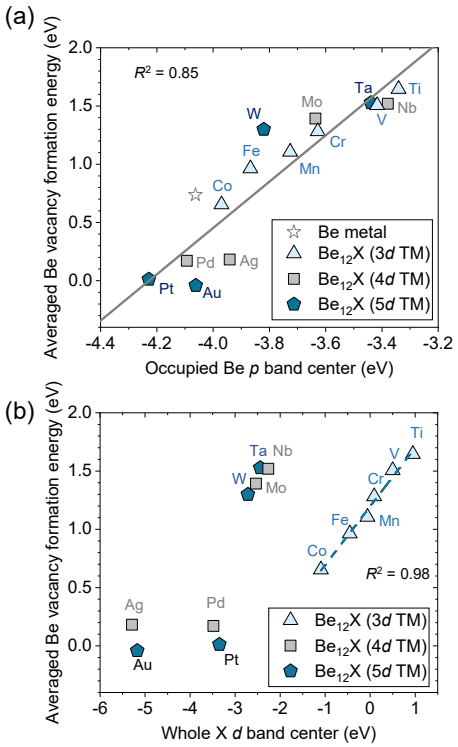

Fig. 5. Plots of Be vacancy formation energy in $Be_{12}X$ (X = Ti, V, Cr, Mn, Fe, Co, Nb, Mo, Pd, Ag, Ta, W, Pt and Au) bulk with (a) occupied Be *p* and (b) whole X-*d* band centers. In panel (a) the plots for $Be_{12}X$ (X: 3*d*, 4*d*, and 5*d* transition metal) were linearly fitted with $R^2 = 0.85$ (R^2: correlation factor). In panel (b), the results of $Be_{12}X$ (X: 3*d* transition metal) intermetallics were linearly fitted, resulting in $R^2 = 0.98$.

The hydrogen solution energy for one interstitial hydrogen atom in $Be_{12}X$ bulk was calculated to assess the hydrogen affinities of Be intermetallics and its possible link with electronic descriptors in a low hydrogen concentration regime. Fig. 6 shows the atomic configurations of interstitial hydrogen atom and the hydrogen solution energies plotted with the group number and occupied Be *p* band center. Three interstitial sites, namely, *i*1, *i*2, and *i*3 sites, were considered for hydrogen accommodation in this study. The interstitial *i*1 site is an octahedral site surrounded by 4 Be atoms at Be3 site, while *i*2 and *i*3 are tetrahedral sites surrounded by 3 Be atoms and 1 X atom (Fig. 6a–c). These sites are known to be the energetically preferable sites for accommodating interstitial hydrogen

atom in $Be_{12}Ti$ bulk.[29,49] The obtained hydrogen solution energies for $Be_{12}X$ were all positive, indicating an endothermic reaction underwent by the hydrogen solution (Fig. 6d). The hydrogen solution energy of the Be metal with a hydrogen atom at the basal tetrahedral site, the most energetically favorable site for interstitial hydrogen in a hexagonal close-packed Be metal,[47] was calculated to be $E_H = 1.64$ eV. Compared with Be metal, the hydrogen solution energies in the intermetallics with early and middle TMs were significantly lower, while those of Be intermetallics with late TMs (i.e. Pd, Pt, Ag, and Au) were found to be comparable or even higher (Fig. 6d). The hydrogen solution energies are plotted with the occupied Be *p* band center in Fig. 6h. The different trend was seen between the octahedral (*i*1 site) and tetrahedral configurations (*i*2 and *i*3 sites), hence trendlines were separately marked for them. This could drive from the higher influence of TM at *i*1 site as the fraction of TM/Be is higher in the octahedral configuration. Note that $Be_{12}W$ was an outlier of the line plot, so the data were not included for the line. For the intermetallics with middle and late TMs located in the left region in Fig. 6e, the trendlines showed linear correlations with the occupied Be *p* band center. However, the linear trends were not applicable to the intermetallics with early TMs (group number < 6), in which hydrogen solution energies were unchanged with the occupied Be *p* band center when it was higher than –3.5 eV.

The energetic difference in hydrogen solution in the $Be_{12}X$ compounds could be qualitatively understood from the PDOS projected onto interstitial hydrogen atom at *i*1 site and neighbor atoms as represented in Fig. 6g–j. By the dissolution, the electronic states projected onto H atom is split into deep-lying filled H *s*–Be *p* bonding state and antibonding states as a result of the interaction with Be and X in the bulk. When X is a noble metal, such as $Be_{12}Au$, bonding of interstitial H is very weak because the peak of

the anti-bonding states is below the Fermi energy and the anti-bonding states are filled (Fig. 6g). The anti-bonding state was upshifted towards the Fermi level and the anti-bonding states was partially filled in $Be_{12}Pd$ (Fig. 6h). On the contrary, the antibonding state were further shifted-up in the intermetallics with early and middle TMs, such as $Be_{12}V$ and $Be_{12}Fe$ (Fig. 6i,j). The low and positive hydrogen solution energies in the $Be_{12}X$ with early and middle TMs indicates a relatively strong chemical bonding between interstitial H atom and the neighbor atoms, which could be attributed to decreased degree of the filling of the anti-bonding states. This interpretation is in line with the *d* band theory for precious metal catalysis.

The lattice volume of $Be_{12}X$ became larger with either early or late TMs (Fig. 1 and Table S1 in SI), leading to longer bond distances and larger space for accommodating interstitial hydrogen atom. However, it was found that the cell volume had a poor correlation with hydrogen solution energy with $R^2 < 0.2$ (Fig. S5 in SI). The hydrogen solution energy had no clear correlation with previously reported electronic descriptors, namely the whole Be *p* band center (Fig. S6 in SI) and whole X *d* band center (Fig. 6f) which have been used for perovskite oxides and precious metal catalysis. This fact indicates that, because of different manner of bonding within $Be_{12}X$ from these materials, the previous descriptors cannot be directly applied to the intermetallics.

In summary, we found that the occupied Be *p* band center is a bulk electric descriptor, correlating with both the Be vacancy formation energy and hydrogen solution energy for $Be_{12}X$. The descriptor is a bulk property and hence directly calculated from existing crystallographic data, which is practical because it does not require surface structure and configuration of interstitial hydrogen atom. The limitation lies in the nonlinear region of the occupied *p* band center with hydrogen solution energy in the large

(less negative) energy region, this may be improved by considering the shape of *p* band as previously done for the *d* band theory.[30,50] Although present study provides insight for material design using a point defect model, it is known that hydrogen isotopes are trapped by vacancy clusters and helium bubbles induced by fast neutron irradiation. Hence the formation process of defect–hydrogen complexes and its correlation with electronic descriptors will be further investigated in our future study for the application. As the required quantity of neutron multiplier is significantly large (e.g., several hundred tons per fusion reactor), the descriptor can help not only to predict chemical properties but also guide information-driven material development using elements with a rich abundance, low cost, and reduced radio-activation character.

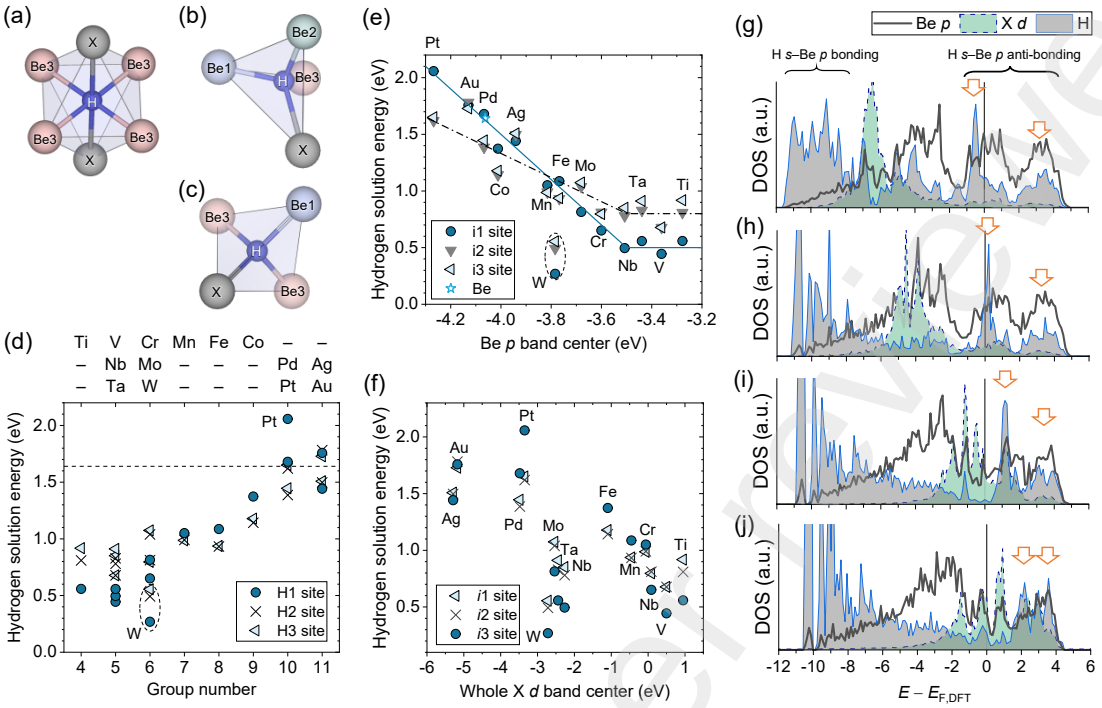

Fig. 6. Hydrogen solution in $Be_{12}X$ (X = Ti, V, Cr, Mn, Fe, Co, Nb, Mo, Pd, Ag, Ta, W, Pt and Au). (a–c) Atomic configurations of hydrogen atom at (a) *i*1, (b) *i*2, and (c) *i*3 sites in $Be_{12}X$ bulk. Hydrogen solution energy plotted with (d) group number, (e) occupied Be *p* band center, and (f) and whole *d* band center. The partial density of states (PDOS) of interstitial hydrogen at *i*1 site and neighbor Be and transition metal atoms in (a) $Be_{12}Au$, (b) $Be_{12}Pd$, (c) $Be_{12}Fe$, and $Be_{12}V$ where arrows represent the peak positions of the H *s*–Be *p* anti-bonding states. In panel (d), horizontal dashed line represents hydrogen solution energy of hydrogen atom at the basal tetrahedral site in Be metal (E_H = 1.64 eV). In panel (e), solid and dashed lines denote linear regressions for hydrogen solution energy at the tetrahedral and octahedral configurations, respectively, in which Be and $Be_{12}W$ are not included.

4. Conclusions

First-principles calculations were performed for existing 42 Be-intermetallics to assess an effective bulk electronic descriptor for Be-rich neutron multiplier. We find that the occupied Be *p* band center referenced with Fermi level is an electric descriptor which correlates with both the Be vacancy formation energy and hydrogen solution energy. The positive and linear correlation was obtained between the Be vacancy formation energy and the occupied Be *p* band center, where correlation factors (R^2) for all of the considered

compounds and $Be_{12}X$ series were 0.65 and 0.85, respectively. It is shown that hydrogen solution energy in $Be_{12}X$ can be lowered with early and middle TMs because of the hybridization of Be *p* states with partially occupied TM *d* states. Contrary, the energies for Be vacancy formation and hydrogen solution were poorly correlated with previously reported electronic descriptors, i.e., the whole *p* band center and whole *d* band centers for the perovskite bulk and catalyst surface, respectively. It is demonstrated that the descriptor directly computed from the crystal structure can be experimentally evaluated by measuring the Be–*K* emissions with a high energy resolution. Therefore, tuning the descriptor can guide the materials development of new Be intermetallic neutron multiplier.

Associated Content

The Supporting Information is available free of charge at https://xxxxx.

Author Information

Corresponding author

Keisuke Mukai: Institute of Advanced Energy, Kyoto University, Gokasho, Uji, Kyoto 611-0011, Japan
k-mukai@iae.kyoto-u.ac.jp
ORCiD: 0000-0001-8067-8732

Authors

Ryuta Kasada: Institute for Material Research, Tohoku University, 2-1-1 Katahira, Aoba-ku, Sendai 980-8577, Japan. ryuta.kasada.e7@tohoku.ac.jp

Kim Jae-Hwan: Fusion Energy Research and Development Directorate, National Institutes for Quantum Science and Technology, 2-166 Obuchi, Omotedate, Rokkasho, Aomori, 039-3212, Japan. kim.jaehwan@qst.go.jp

Masaru Nakamichi: Fusion Energy Research and Development Directorate, National Institutes for Quantum Science and Technology, 2-166 Obuchi, Omotedate, Rokkasho, Aomori, 039-3212, Japan. nakamichi.masaru@qst.go.jp

Notes

The authors declare no competing financial interest.

Acknowledgement

This work was financially supported by a Grant-in-Aid for young scientists (20K14442)

from the Japan Society for the Promotion of Science (JSPS) and Japan Science and Technology Agency (JST) COI-NEXT program for mineral recycling system and society driven by innovative refining technology (JPMJPF2002). The computations were carried out using the JFRS-1 supercomputer system at Computational Simulation Centre of International Fusion Energy Research Centre (IFERC-CSC) in Rokkasho Fusion Institute of QST (Aomori, Japan).

References

[1] B. Hammer, J.K. Nørskov, Why gold is the noblest of all the metals, Nature. 376 (1995) 238–240. https://doi.org/10.1038/376238a0.

[2] B. Hammer, J.K. Nørskov, Electronic factors determining the reactivity of metal surfaces, Surf. Sci. 343 (1995) 211–220. https://doi.org/10.1016/0039-6028(96)80007-0.

[3] B. Hammer, J.K. Nørskov, Theoretical surface science and catalysis—calculations and concepts, Adv. Catal. 45 (2000) 71–129. https://doi.org/10.1016/S0360-0564(02)45013-4.

[4] X. Shen, Y. Pan, B. Liu, J. Yang, J. Zeng, Z. Peng, More accurate depiction of adsorption energy on transition metals using work function as one additional descriptor, Phys. Chem. Chem. Phys. 19 (2017) 12628–12632. https://doi.org/10.1039/c7cp01817g.

[5] H. Xin, A. Vojvodic, J. Voss, J.K. Nørskov, F. Abild-Pedersen, Effects of d-band shape on the surface reactivity of transition-metal alloys, Phys. Rev. B. 89 (2014) 1–5. https://doi.org/10.1103/PhysRevB.89.115114.

[6] S. Bhattacharjee, U. V. Waghmare, S.C. Lee, An improved d-band model of the catalytic activity of magnetic transition metal surfaces, Sci. Rep. 6 (2016) 1–10. https://doi.org/10.1038/srep35916.

[7] Z.W. She, J. Kibsgaard, C.F. Dickens, I. Chorkendorff, J.K. Nørskov, T.F. Jaramillo, Combining theory and experiment in electrocatalysis: Insights into materials design, Science (80-.). 355 (2017) eaad4998. https://doi.org/10.1126/science.aad4998.

[8] Y. Zheng, Y. Jiao, M. Jaroniec, S.Z. Qiao, Advancing the electrochemistry of the hydrogen-Evolution reaction through combining experiment, Angew. Chemie - Int. Ed. 54 (2015) 52–65. https://doi.org/10.1002/anie.201407031.

[9] T. Kimata, K. Kakitani, S. Yamamoto, I. Shimoyama, D. Matsumura, A. Iwase, W. Mao, T. Kobayashi, T. Yamaki, T. Terai, Activity enhancement of platinum oxygen-reduction electrocatalysts using ion-beam induced defects, Phys. Rev. Mater. 6 (2022) 035801. https://doi.org/10.1103/PhysRevMaterials.6.035801.

[10] J.H. Lee, D. Yim, J.H. Park, C.H. Lee, J.M. Ju, S.U. Lee, J.H. Kim, Tuning d-band centers by coupling PdO nanoclusters to WO_3 nanosheets to promote the oxygen reduction reaction, J. Mater. Chem. A. 8 (2020) 13490–13500. https://doi.org/10.1039/d0ta02840a.

[11] H. Tao, S. Liu, J.L. Luo, P. Choi, Q. Liu, Z. Xu, Descriptor of catalytic activity of metal sulfides for oxygen reduction reaction: A potential indicator for mineral flotation, J. Mater. Chem. A. 6

(2018) 9650–9656. https://doi.org/10.1039/c8ta01241e.

[12] L. Giordano, T.M. Østergaard, S. Muy, Y. Yu, N. Charles, S. Kim, Y. Zhang, F. Maglia, R. Jung, I. Lund, J. Rossmeisl, Y. Shao-Horn, Ligand-Dependent Energetics for Dehydrogenation: Implications in Li-Ion Battery Electrolyte Stability and Selective Oxidation Catalysis of Hydrogen-Containing Molecules, Chem. Mater. 31 (2019) 5464–5474. https://doi.org/10.1021/acs.chemmater.9b00767.

[13] Y.L. Lee, J. Kleis, J. Rossmeisl, S.H. Yang, D. Morgan, Prediction of solid oxide fuel cell cathode activity with first-principles descriptors, Energy Environ. Sci. 4 (2011) 3966–3970. https://doi.org/10.1039/c1ee02032c.

[14] A. Grimaud, K.J. May, C.E. Carlton, Y.L. Lee, M. Risch, W.T. Hong, J. Zhou, Y. Shao-Horn, Double perovskites as a family of highly active catalysts for oxygen evolution in alkaline solution, Nat. Commun. 4 (2013) 1–7. https://doi.org/10.1038/ncomms3439.

[15] R. Jacobs, T. Mayeshiba, J. Booske, D. Morgan, Material Discovery and Design Principles for Stable, High Activity Perovskite Cathodes for Solid Oxide Fuel Cells, Adv. Energy Mater. 8 (2018) 1–12. https://doi.org/10.1002/aenm.201702708.

[16] R. Jacobs, J. Hwang, Y. Shao-Horn, D. Morgan, Assessing Correlations of Perovskite Catalytic Performance with Electronic Structure Descriptors, Chem. Mater. 31 (2019) 785–797. https://doi.org/10.1021/acs.chemmater.8b03840.

[17] T.T. Mayeshiba, D.D. Morgan, Factors controlling oxygen migration barriers in perovskites, Solid State Ionics. 296 (2016) 71–77. https://doi.org/10.1016/j.ssi.2016.09.007.

[18] R.B. Wexler, G.S. Gautam, E.B. Stechel, E.A. Carter, Factors Governing Oxygen Vacancy Formation in Oxide Perovskites, J. Am. Chem. Soc. 143 (2021) 13212–13227. https://doi.org/10.1021/jacs.1c05570.

[19] N. Ohba, T. Yokoya, S. Kajita, K. Takechi, Search for high-capacity oxygen storage materials by materials informatics, RSC Adv. 9 (2019) 41811–41816. https://doi.org/10.1039/c9ra09886k.

[20] S.C. Middleburgh, R.W. Grimes, Defects and transport processes in beryllium, Acta Mater. 59 (2011) 7095–7103. https://doi.org/10.1016/j.actamat.2011.07.064.

[21] G.D. Samolyuk, P.D. Edmondson, First principles study of the stability and thermal conductivity of novel Li-Be hybrid ceramics, Acta Mater. 215 (2021) 117052. https://doi.org/10.1016/j.actamat.2021.117052.

[22] M. Nakamichi, J.H. Kim, Fabrication and hydrogen generation reaction with water vapor of prototypic pebbles of binary beryllides as advanced neutron multiplier, Fusion Eng. Des. 98–99 (2015) 1838–1842. https://doi.org/10.1016/j.fusengdes.2015.04.026.

[23] M.M. Nakamura, J.H. Kim, M. Nakamichi, Y. Someya, K. Tobita, Y. Sakamoto, R. Hiwatari, Modeling of chemical reactions of beryllium/beryllide pebbles with steam for hydrogen safety design of water-cooled DEMO, Fusion Eng. Des. 136 (2018) 1484–1488.

https://doi.org/10.1016/j.fusengdes.2018.05.039.

[24] S. Konishi, M. Enoeda, M. Nakamichi, T. Hoshino, A. Ying, S. Sharafat, S. Smolentsev, Functional materials for breeding blankets—status and developments, Nucl. Fusion. 57 (2017) 092014. https://doi.org/10.1088/1741-4326/aa7e4e.

[25] V. Chakin, R. Rolli, A. Moeslang, P. Kurinskiy, Tritium and helium release from highly neutron irradiated titanium beryllide, Fusion Eng. Des. 98–99 (2015) 1728–1732. https://doi.org/10.1016/j.fusengdes.2015.01.038.

[26] V. Chakin, R. Rolli, R. Gaisin, U. Hoeppener-Kramar, M. Nakamichi, M. Zmitko, Tritium release and retention in beryllium and titanium beryllide after neutron irradiation up to damage doses of 23-38 dpa, Fusion Eng. Des. 161 (2020) 111938. https://doi.org/10.1016/j.fusengdes.2020.111938.

[27] J. Kim, T. Hwang, S. Nakano, M. Miyamoto, H. Iwakiri, M. Nakamichi, Deuterium desorption and retention of Beryllium intermetallic compounds for fusion applications, J. Nucl. Mater. 550 (2021) 152936. https://doi.org/10.1016/j.jnucmat.2021.152936.

[28] D. V. Bachurin, C. Stihl, P. V. Vladimirov, Ab initio study of hydrogen diffusion in Be and $Be_{12}Ti$ for fusion applications, Comput. Mater. Sci. 187 (2021). https://doi.org/10.1016/j.commatsci.2020.109921.

[29] Y. Fujii, M. Miyamoto, J.H. Kim, M. Nakamichi, N. Murayoshi, H. Iwakiri, Hydrogen retention behavior of beryllides as advanced neutron multipliers, Nucl. Mater. Energy. 9 (2016) 233–236. https://doi.org/10.1016/j.nme.2016.03.001.

[30] D. V. Bachurin, P. V. Vladimirov, Ab initio study of Be and $Be_{12}Ti$ for fusion applications, Intermetallics. 100 (2018) 163–170. https://doi.org/10.1016/j.intermet.2018.06.009.

[31] V. Chakin, R. Rolli, R. Gaisin, P. Kurinskiy, J.H. Kim, M. Nakamichi, Effect of heat treatment of titanium beryllide on tritium/hydrogen release, Fusion Eng. Des. 137 (2018) 165–171. https://doi.org/10.1016/j.fusengdes.2018.09.005.

[32] J.H. Kim, M. Nakamichi, Characterization of modified $Be_{13}Zr$ beryllide pebbles as advanced neutron multipliers, Fusion Eng. Des. 146 (2019) 2608–2612. https://doi.org/10.1016/j.fusengdes.2019.04.054.

[33] J.H. Kim, M. Nakamichi, Synthesis and characteristics of ternary Be-Ti-V beryllide pebbles as advanced neutron multipliers, Fusion Eng. Des. 109–111 (2016) 1764–1768. https://doi.org/10.1016/j.fusengdes.2015.09.015.

[34] J.H. Kim, M. Nakamichi, Fabrication and characterization of Be-Zr-Ti ternary beryllide pebbles, Fusion Eng. Des. 136 (2018) 864–868. https://doi.org/10.1016/j.fusengdes.2018.04.024.

[35] J.H. Kim, M. Nakamichi, Reactivity and thermal stability of ternary Be-Zr-V beryllides, Fusion Eng. Des. 146 (2019) 357–360. https://doi.org/10.1016/j.fusengdes.2018.12.067.

[36] P.A. Burr, S.C. Middleburgh, R.W. Grimes, Crystal structure, thermodynamics, magnetics and

disorder properties of Be-Fe-Al intermetallics, J. Alloys Compd. 639 (2015) 111–122. https://doi.org/10.1016/j.jallcom.2015.03.101.

[37] P.A. Burr, S.C. Middleburgh, R.W. Grimes, Solubility and partitioning of impurities in Be alloys, J. Alloys Compd. 688 (2016) 382–385. https://doi.org/10.1016/j.jallcom.2016.07.014.

[38] M.L. Jackson, P.A. Burr, R.W. Grimes, Defect processes in $Be_{12}X$ (X = Ti, Mo, V, W), Nucl. Fusion. 57 (2017) 086049. https://doi.org/10.1088/1741-4326/aa7b41.

[39] K. Mukai, R. Kasada, K. Yabuuchi, S. Konishi, J.-H. Kim, M. Nakamichi, Valence Electron and Chemical State Analysis of $Be_{12}M$ (M = Ti, V) Beryllides by Soft X-ray Emission Spectroscopy, ACS Appl. Energy Mater. 2 (2019) 2889–2895. https://doi.org/10.1021/acsaem.9b00223.

[40] F. Izumi, K. Momma, Three-dimensional visualization in powder diffraction, Solid State Phenom. 130 (2007) 15–20. https://doi.org/10.4028/www.scientific.net/SSP.130.15.

[41] M. Terauchi, H. Takahashi, N. Handa, T. Murano, M. Koike, T. Kawachi, T. Imazono, M. Koeda, T. Nagano, H. Sasai, Y. Oue, Ultrasoft-X-ray emission spectroscopy using a newly designed wavelength-dispersive spectrometer attached to a transmission electron microscope, J. Electron Microsc. (Tokyo). 61 (2012) 1–8. https://doi.org/10.1093/jmicro/dfr076.

[42] G. Kresse, J. Furthmüller, Efficient iterative schemes for ab initio total-energy calculations using a plane-wave basis set, Phys. Rev. B. 54 (1996) 11169–11186. https://doi.org/10.1103/PhysRevB.54.11169.

[43] P.E. Blöchl, Projector augmented-wave method, Phys. Rev. B. 50 (1994) 17953–17979. https://doi.org/10.1103/PhysRevB.50.17953.

[44] J.P. Perdew, K. Burke, M. Ernzerhof, Generalized gradient approximation made simple, Phys. Rev. Lett. 77 (1996) 3865–3868. https://doi.org/10.1103/PhysRevLett.77.3865.

[45] National Institute for Materials Science (NIMS) AtomWork, (n.d.). http://crystdb.nims.go.jp/.

[46] K. Momma, F. Izumi, VESTA 3 for three-dimensional visualization of crystal, volumetric and morphology data, J. Appl. Crystallogr. 44 (2011) 1272–1276. https://doi.org/10.1107/S0021889811038970.

[47] M.G. Ganchenkova, V.A. Borodin, R.M. Nieminen, Hydrogen in beryllium: Solubility, transport, and trapping, Phys. Rev. B. 79 (2009) 1–11. https://doi.org/10.1103/PhysRevB.79.134101.

[48] N. Wilson, C. MacRae, A. Torpy, Fundamental aspects of SXES in the Quantification of Minerals and Materials, Microsc. Microanal. 27 (2021) 1368–1369. https://doi.org/10.1017/s1431927621005092.

[49] X. Zhu, C. Wang, J. Liu, X. Zhang, H. Deng, W. Duan, L. Yang, Retention and diffusion of transmutation H and He atoms in $Be_{12}Ti$: first-principles calculations, RSC Adv. 8 (2018) 35735–35743. https://doi.org/10.1039/c8ra06768f.

[50] X.S. Kong, S. Wang, X. Wu, Y.W. You, C.S. Liu, Q.F. Fang, J.L. Chen, G.N. Luo, First-principles calculations of hydrogen solution and diffusion in tungsten: Temperature and defect-

trapping effects, Acta Mater. 84 (2015) 426–435. https://doi.org/10.1016/j.actamat.2014.10.039.

Graphical Abstract